MAGNETOHYDRODYNAMICS Vol. 59 (2023), No. 3-4, pp. 401–413
DOI: 10.22364/mhd.59.3-4.12

NUMERICAL STUDY OF THE BRIDGMAN DIRECTIONAL SOLIDIFICATION PROCESS OF PHOTOVOLTAIC SILICON INGOT USING POWER CONTROL TECHNIQUE

Brahim Hiba [1*], *Abdallah Nouri* [1], *Lakhdar Hachani* [1], *Kader Zaidat* [2],

[1] *Laboratoire Physique de Matériaux, Université Amar Telidji de Laghouat, BP 37 G Boulevard des martyrs, Laghouat 03000, Algérie*
[*] *e-Mail: b.hiba@ens-lagh.dz*
[2] *SIMAP-EPM PHELMA, University of Grenoble Alpes, BP 75, 38402 Saint-Martin-d'Hères Cedex, France*

This work is concerned with the improvement of silicon photovoltaic solar cells using electromagnetic stirring in prior processing by controlling the hydrodynamics of the silicon bath during ingot solidification. The vertical Bridgman directional solidification furnace called VB2 was numerically investigated using a controlled power-down technique under forced convection generated by a travelling magnetic field, i.e. a full 3D numerical model of the VB2 furnace has been developed using the Comsol MultiphysicsTM software. Enthalpy formulation based on fixed-grid techniques is used for the phase-change phenomena considering magnetohydrodynamic forced convection created by a Lorentz force generated by a specific cylindrical Bitter coil. The model provides the temperature distribution in the entire furnace as well as specific details regarding the solidification process (i.e. solidification fraction and solid-liquid interface shape), flow patterns and melt velocities. The obtained numerical results show good consistency with experimental measurements and analysis, on the one hand, and can be considered as useful orientation to improve the solidification process, on the other hand. It is shown that the travelling magnetic field acting in the melt drives a moderately turbulent flow which has a significant impact on the solid-liquid interface in terms of morphology and symmetry during silicon solidification and, consequently, on the tight control of the crystallization process that can affect the silicon crystal morphology and impurity distributions.
Keywords: Electromagnetic stirring, polycrystalline photovoltaic silicon, solid-liquid interface, travelling magnetic field, vertical Bridgman directional solidification.

Introduction. Polycrystalline silicon is one of the most widely used materials for the production of photovoltaic solar cells. In order to ensure the high efficiency of final cells, a silicon feedstock of high purity must be used. To reduce costs, it is possible to start with readily available solar grade metallurgical silicon feedstock applying an appropriate directional solidification process to produce ingots [1]. However, the raw material used for the photovoltaic polycrystalline silicon ingot production by the actual directional solidification process contains impurities that have a major impact on the final ingot and, therefore, on the performance of the solar cells, where they can decrease their efficiency [2–3]. To enhance the quality of the final ingot, i.e. the impurities' distribution and crystal structure, it is necessary to control the factors that affect it during the solidification process as the growth rate, the temperature gradient, the cooling rate and the hydrodynamic motion of the silicon melt. Controlling mainly the configuration of the melt and the thermal configuration of the furnace should lead to a better control of the solid-liquid interface shape and, therefore, the segregation of impurities and crystal structure during directional solidification [4].

The use of electromagnetic stirring (EMS) to control the melt flow in the case of conductive charge in the liquid phase has become an interesting technique. However, the configuration of the MHD flow pattern strongly depends on the design of the electromagnetic inductor which is the source of creation, distribution and action of the Lorentz

force in the silicon bath. For a cylindrical system with a symmetry axis (i.e. a travelling magnetic field (TMF) apparatus used in the VB2 furnace), the choice of 2D models to simulate melt flow driven by the TMF during the solidification process which is obviously based on an axisymmetric approach does not always predict the real existing MHD flow configuration. On this basis, Cablea *et al.* [1, 5, 8] numerically examined the effect of two TMF configurations (upward and downward) at the solid-liquid interface in a vertical Bridgman directional solidification experiment (VB2 furnace) using a 2D axisymmetric model. As a result, two possible regular shapes of the solid-liquid interface – convex and concave – were observed from the solid, depending on the TMF direction stirring upward or downward, respectively. However, our recent 3D numerical investigation [7], focused on the analysis of the MHD flow configuration and instability under identical experimental conditions of the VB2 furnace, has confirmed that the real topology of the MHD flow is not always axisymmetric but only can be adapted to quasi-symmetric with respect to a specific meridional plane. In fact, this paper is part of an extensive continuity of our previous work with an improved approach for solidification (i.e. phase change problem) under the action of electromagnetic stirring, which primary objective will be focused on a 3D numerical study using the real TMF apparatus (Bitter coil, Figs. 1,3) supposed to be more predictive rather than using a 2D modelling method to examine the impact of electromagnetic stirring on the flow configuration as well as on the stability and shape of the solid-liquid interface during the solidification of silicon under power down control technique.

1. Experimental process.

The VB2 setup is a cylindrical resistive furnace, where a benchmark of the vertical Bridgman solidication experiment is to obtain cylindrical polycrystalline silicon ingots of 2 inches in diameter. It was performed at the SIMaP/EPM Laboratory in Grenoble, France.

As shown in Fig. 1, the VB2 furnace is composed of three principal parts: two graphite resistors (top and bottom), surrounded by thermal insulation of graphite foam and in between there is an adiabatic zone to improve the control of the radial and vertical thermal gradients in the silicon melt. The two resistors are in form of electrical

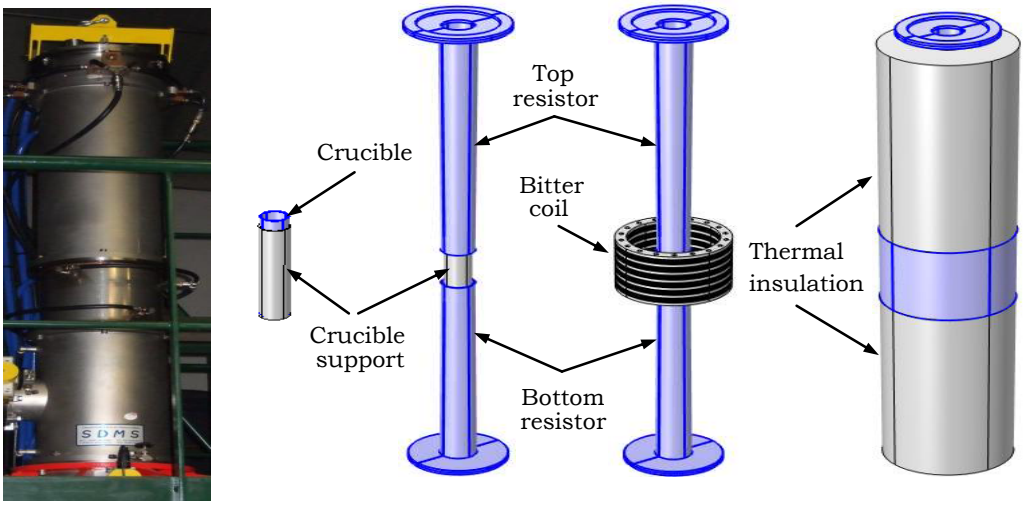

Fig. 1. Main components of the VB2 furnace (SIMaP/EPM Laboratory, Grenoble, France).

heaters in graphite; they can generate a controlled thermal heat flux as well as an applied temperature gradient $\Delta T_{\text{furnace}}$ and a cooling rate C_{r} using the electrical power down control technique. The principle of the electrical power down control technique is to solidify a fixed silicon ingot (i.e. without pulling devices) between two adjacent resistors that are temperature-controlled. Thus, upon creating an initial gradient between the two resistors, directional solidification is performed by decreasing the temperatures of both resistors with the same or different cooling rate. Since electrical heating devices are used to control the furnace temperature by a control system, the term "power reduction" means the required decrease in power to solidify the silicon ingot.

In the central adiabatic region, the solar metallurgical grade silicon is placed in a cylindrical fused silica crucible of 5 cm in diameter, which is partially filled (12 cm high) and held by a graphite support surrounded by multi-layer foam insulation. In addition, an electromagnetic Bitter coil generating an external travelling magnetic field (TMF) is used to control the MHD flow of the silicon melt during the solidification process without contaminating it. The Bitter coil apparatus has the height $H_{\text{IN}} = 18\,\text{cm}$ and internal and external diameters of 20 and 25 cm, respectively. The TMF is characterized by the wavelength λ_0 and the pole pitch τ, where $\lambda_0 = 2\tau = 168\,\text{mm}$, so that the wave number $K = 2\pi/\lambda_0 = 37.4\,\text{m}^{-1}$. The coils of the Bitter coil has six blocks of discs, each block having a stack of ten individual copper discs with Kapton electrical insulation. The TMF system is powered by three-phase currents shifted by $2\pi/3$ at the network frequency $f_0 = 50\,\text{Hz}$. The power down control technique is used for the top and bottom resistive graphite resistors with an applied thermal gradient to ensure a vertical direction solidification process of the silicon melt.

2. Numerical model.

The full 3D multi-disciplinary developed model, dealing with the whole VB2 furnace, is governed by a non-linear coupling set of equations, including electromagnetism, fluid mechanics, and heat transfer with phase change phenomena, as detailed below.

2.1. Electromagnetic part. This part solves the set of Maxwell's equations in a harmonic mode for different coils composing the Bitter coil based on the A-V potential formulation and considering the Coulomb gauge condition ($\nabla \mathbf{A} = 0$) to calculate the generated TMF and subsequently the Lorentz force induced in the silicon liquid charge. With the basic assumption that the displacement current is neglected in the usual frequency range ($|\mathbf{J}| \gg (\partial E/\partial t)$), following [9], the differential equations governing that method are

$$\nabla \times \mathbf{H} = \mathbf{J} = \mathbf{J}_{\text{s}} + \mathbf{J}_{\text{i}}, \tag{1}$$

$$\nabla \times \left(\mu_{\text{e}}^{-1}\right) \nabla \times \mathbf{A} + \sigma_{\text{e}} \left(\frac{\partial \mathbf{A}}{\partial t} + \nabla V \right) = \mathbf{J}_{\text{s}}, \tag{2}$$

$$\nabla \cdot \left(\sigma_{\text{e}} \left(\frac{\partial \mathbf{A}}{\partial t} + \nabla V \right) \right) = 0, \tag{3}$$

where $\mathbf{H}$ is the magnetic field intensity vector, $\mathbf{J}$ is the total current density vector, $\mathbf{J}_{\text{s}}$ is the applied source of the current density vector, $\mathbf{J}_{\text{i}} = \sigma_{\text{e}}(\mathbf{E} + \mathbf{u} \times \mathbf{B})$ is the induced current density, $\mathbf{E}$ is the electric field intensity vector, $\mathbf{B}$ is the induced magnetic field; $\mathbf{u}$ is the melt velocity, $\mathbf{A}$ is the magnetic vector potential, V is the electric scalar potential, σ_{e} is the electric conductivity, $\mu_{\text{e}} = \mu_0 \mu_r$ is the magnetic permeability; μ_0 is the permeability of free space, and μ_r is the relative permeability.

The continuity equation for the electric current follows from taking the divergence of both sides of Eq. (1),

$$\nabla \cdot \mathbf{J} = 0 \tag{4}$$

Also, the advection of the magnetic field by the liquid metal velocity can be neglected due to the low Reynolds magnetic number $\mathrm{Rm} = \mu_0 \sigma u_\mathrm{l} \approx 0.001$, where u is taken as the maximum velocity $u = \|u_{max}\| = 3.4\,\mathrm{cm/s}$ and l is a typical length scale of the flow assumed in the considered case as the radius of the crucible ($l \equiv R$). As well known, when $\mathrm{Rm} \ll 1$, the electromagnetic aspect of the problem separates from the liquid metal flow, allowing for independent solutions to be obtained. Thus, the induced current density takes the following form,

$$\mathbf{J}_\mathrm{i} = \sigma_\mathrm{e} \mathbf{E} \tag{5}$$

and when the harmonic approach is used, all equations for the complex amplitudes of the electromagnetic quantities are solved.

The time average Lorenz force density value is

$$\langle F_{Ltz} \rangle = \frac{1}{2} \left(J_r \cdot B_r + J_\mathrm{i} \cdot B_\mathrm{i} \right), \tag{6}$$

where the subscripts 'i' and 'r' denote the imaginary and the real part of the complex value.

2.2. Fluid mechanics part. A realizable k-ε turbulent model was adopted to treat the fluid flow under electromagnetic stirring. This model of two equations (k – turbulent kinetic energy and ε – turbulent dissipation) with Reynolds averaged modelling can provide an accurate result for the mean flow velocity and does not require much of the computational power [10]. The reader can refer to Hiba *et al.* [6–7] for further details concerning the turbulent model adopted to resolve the set of magnetohydrodynamic equations, fundamentally based on low frequency and low magnetic induction, and on an averaged expression of the Lorentz force. The liquid was assumed to be incompressible with a constant density and viscosity. The no-slip flow boundary condition was applied to the silicon melt. The thermodynamic/physical properties of the silicon charge used in the current simulations are listed in Table 1.

2.2.1. Governing equations. With the specific design of the VB2 furnace configuration, the bottom zone is cold and the top zone is hot with quasi absence of thermal gradients in the radial direction (i.e. incompressible fluids with constant density), and there is no effect of buoyancy forces. This means that the driving force stirring the melt is only the Lorentz force given by Eq. (6). Thus, the momentum equation of MHD flow for this case with a phase change can be expressed as follows:

$$\rho_\mathrm{l} \left[\frac{\partial (\mathbf{u})}{\partial t} + \frac{1}{f_\mathrm{l}} (\mathbf{u} \cdot \nabla) \mathbf{u} \right] - \nabla \cdot (\mu_\mathrm{l} \cdot \nabla \cdot \mathbf{u}) + S(T)\,\mathbf{u} = -f_\mathrm{l} \nabla (p) + f_\mathrm{l} \langle F_{LTZ} \rangle, \tag{7}$$

with the continuity equation

$$\nabla \cdot \mathbf{u} = 0, \tag{8}$$

where $\mathbf{u} = f_\mathrm{l} \mathbf{u}_\mathrm{l}$ is the intrinsic velocity in the liquid phase.

2.2.2. The way of considering the presence of solid phase. For silicon phase change modelling, the enthalpy formulation based on a fixed-grid approach is adopted to predict the solidification process in terms of the solid-liquid interface location, morphology and its progression in the ingot. This latter is part of uni-domain approaches, where the same

and unique system of equations is solved everywhere in the domain containing both the solid and liquid phases which are represented by a single fluid. A major advantage is that the method does not require explicit treatment of the moving boundary. Enthalpy methods basically account for latent heat in energy equations by allocating a nodal latent heat value to each numerical cell based on the cell temperature. However, the distinction between solid and liquid poses a numerical difficulty because the properties of pure material change immediately at the melting temperature T_{m}. In order to circumvent convergence problems, a mushy zone approach was adopted, where the thermophysical properties of the solid and liquid phases are spread over a user-defined melting temperature range ΔT (in our study $\Delta T = 1\,\mathrm{K}$). Moreover, an important basic assumption with fixed-grid solution techniques is that the establishment of a zero-velocity condition is needed in cells when the liquid area becomes solid. Numerous methods may be used, in principle, to "switch off" velocities in computing cells that are freezing (or "turn on" velocities in the case of melting). The momentum equation part of the study requires an additional modelling term $S(T)u$ in the momentum equation (7), accounting for the porosity of the mushy zone. The porosity function $S(T)$ is a sink-term in the momentum equation derived from the Carman–Kozeny equation (9). In the case of a solid fraction, the momentum equation provides a trivial ($u = 0$) solution to ensure immobility. The simulating term

$$S(T) = A_{\mathrm{mush}} \frac{(1 - f_{\mathrm{l}})^2}{f_{\mathrm{l}}^3 + \varepsilon_0} \tag{9}$$

overrides any other term in the momentum equation in the solid zone [11, 12]; the mushy zone constant is $A_{\mathrm{mush}} = 10^6\,\mathrm{kg/(m^3 s}$, f_{l} is the liquid fraction defined by Eq. (15), and $\varepsilon_0 = 10^{-3}$ is a small positive calculation constant defined to avoid division by zero in the liquid state ($f_{\mathrm{l}} = 1$).

2.3. Global heat transfer with phase change part. The energy part concerning the heat transfer in the whole furnace, considers all the existing energy exchange mechanisms: conduction, convection and radiation. It is important to mention that the heat source resulting from the Joule effect was included as a source term in the heat transfer in solid dealing with the two graphite resistors, and it was neglected in the silicon material (i.e. electromagnetic heat induction) due to the used low network frequency (50 Hz), which translates much more into a dynamic effect (i.e. electromagnetic stirring).

2.3.1. Heat transfer in the silicon domain with phase change. The heat transfer process in silicon which undergoes a phase change is governed by Eq. (10), taking into account simultaneously the coexistence of both liquid and solid phases. It is no longer possible to describe the position of the interface in detail on a microscopic scale. The liquid-solid transition zone is determined implicitly by the solid fraction function f_{s}. The approach implies defining a single temperature field for the liquid and solid assembly (or enthalpy of the mixture) by determining a specific heat C_p modified by the release of the latent heat L in the temporal variation term,

$$\frac{\partial\left(\rho C_{\mathrm{p}} T\right)}{\partial t} + \frac{\partial\left(\rho f_{\mathrm{l}} L\right)}{\partial t} = -\nabla\left(\rho u h\right) + \nabla\left(\lambda \nabla T\right) \tag{10}$$

where ρ is the density, λ is the thermal conductivity, and the unsteady latent heat L content term in the left side of Eq. (10) is equal to zero for $T < T_{\mathrm{m}} - \Delta T/2$ and $T > T_{\mathrm{m}} + \Delta T/2$ (it affects the energy equation only within a user defined temperature

range ΔT), with

$$\begin{cases} \rho = f_{\mathrm{s}}\rho_{\mathrm{s}} + f_{\mathrm{l}}\rho_{\mathrm{l}}, \\ \lambda = f_{\mathrm{s}}\lambda_{\mathrm{s}} + f_{\mathrm{l}}\lambda_{\mathrm{l}}. \end{cases} \tag{11}$$

The enthalpy of the material is calculated as the sum of the latent heat L and sensible enthalpy,

$$h = \begin{cases} C_{\mathrm{ps}}T & \text{for } T \le T_{\mathrm{m}}, \\ C_{\mathrm{pl}}T + f_{\mathrm{l}}L & \text{for } T > T_{\mathrm{m}}. \end{cases} \tag{12}$$

The specific heat is expressed as a function of the latent heat L and Dirac distribution function $D(T)$ as follows,

$$C_{\mathrm{p}}(T) = C_{\mathrm{ps}} + f_{\mathrm{l}}(T)(C_{\mathrm{pl}} - C_{\mathrm{ps}}) + D(T)L, \tag{13}$$

where $D(T)$ is determined by the melting temperature T_{m}, generally considered to be distributed over a temperature interval of $2\Delta T$ around T_{m} to ensure a smooth transition between the heat capacity values from the liquid to the solid phase [13],

$$D(T) = \frac{1}{\sqrt{\pi}\Delta T/4} \exp\left\{ -\left(\frac{T - T_{\mathrm{m}}}{\Delta T/4} \right)^2 \right\} \tag{14}$$

and

$$f_{\mathrm{l}} = \begin{cases} 1 & \text{for } T > T_{\mathrm{m}} + \Delta T/2, \\ \dfrac{T - (T_{\mathrm{m}} - \Delta T/2)}{\Delta T} & \text{for } T_{\mathrm{m}} + \Delta T/2 \ge T \ge T_{\mathrm{m}} - \Delta T/2, \\ 0 & \text{for } T < T_{\mathrm{m}} - \Delta T/2, \end{cases} \tag{15}$$

with T_{m} being the melting temperature of silicon and ΔT the half-width of the temperature transition.

2.3.2. Heat transfer in the solid furnace parts. In the solid furnace parts, the governing heat transfer equations can be expressed as

$$\frac{\partial(\rho C_{\mathrm{p}}T)}{\partial t} = \nabla(\lambda \nabla T) + Q_{\mathrm{elec}}, \tag{16}$$

with

$$Q_{\mathrm{elec}} = \begin{cases} \dfrac{J^2}{2\sigma_{\mathrm{resistor}}} & \text{in the graphite resistors,} \\ 0 & \text{other solid parts,} \end{cases} \tag{17}$$

and

$$Q_{\mathrm{rad}} = FA\sigma\epsilon\left(T_1^4 - T_2^4\right) \tag{18}$$

with F being the radiation configuration factor; $\sigma = 5.67 \times 10^{-8}\,\mathrm{J/(s{\cdot}m^2K^4)}$ is the Stefan–Boltzmann constant, A is the surface area of the object, and ϵ is the emissivity of the object.

The phase change domain includes a silicon charge in a cylindrical crucible of 12 cm in height and 5 cm in diameter. Different results were obtained, however, in this study; the focus was first on the temperature field for validation purposes of the thermal boundary conditions used in the experiment, then a numerical investigation of the topology of the melt flow field was carried out resulting as well in its effect on the shape, instability and change of the position of the solidification front over time (i.e. solid-liquid interface).

Table 1. Thermo-physical properties of pure silicon [1].

Property	Value	Units
Solid silicon		
Density ρ_s	2310	kg/m^3
Thermal conductivity λ_s	19	W(m·K)
Specific heat C_{ps}	1032	J/(kg·K)
Melting temperature, T_m	1687	K
Liquid silicon		
Density, ρ_l	2560	kg/m^3
Thermal conductivity, λ_l	56.5	W(m·K)
Specific heat, C_{pl}	1032	J/(kg·K)
Dynamic viscosity, μ_l	$7.5{\cdot}10^{-4}$	Pa·s
Latent heat, L	$1.8{\cdot}10^{6}$	J/kg
Electrical conductivity,σ_e	$1.5385{\cdot}10^{6}$	S/m

3. Results and discussions.

In the present study, we deal with the solidification of silicon using a specific cooling system controlled by the power down technique. More details about the experiment and related results can be found in [1, 8].

3.1. Treatment of experimental boundary conditions. It should be emphasized that in the experiment, the temperature boundary conditions prior the solidification as well as the cooling process during solidification were programmed and controlled by the electrical resistor heaters in graphite. Moreover, due to the high melting temperature of silicon, the experimental setup cannot provide precise information needed for the boundary conditions (i.e. exact temperature proles in the crucible and in the silicon

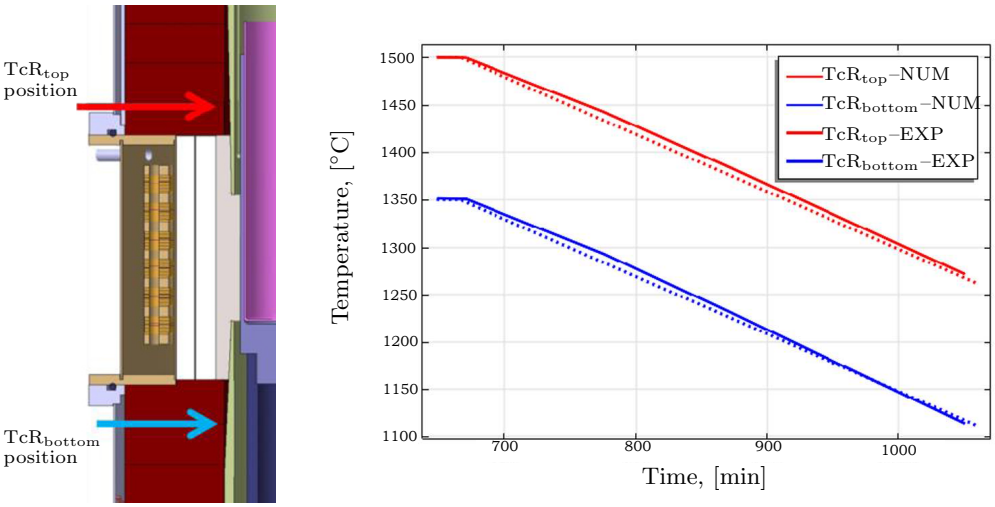

(*a*) (*b*)

Fig. 2. (*a*) Close-up view in the central part of the VB2 furnace with highlighted thermocouples positions, heaters and insulating layers. (*b*) Numerical and experimental results of temperatures of two thermocouples TcR$_{top}$ and TcR$_{bottom}$ during solidification with a cooling rate of 10^{-2} K/s [1].

melt) for such full model; the entire furnace geometry was reproduced in the numerical model, not only the solidication region. Fig. 2*a* depicts a close-up view in the central region of the VB2 furnace, where the two graphite heaters and the insulating layers are highlighted. The approach for the numerical model validation was a direct comparison with experimental measurements.

Using the thermocouples attached to the graphite foam support at different heights, namely, the temperatures of the two resistors ($\mathrm{TcR_{top}}$ and $\mathrm{TcR_{bottom}}$) were measured. The measured temperatures and the simulated temperatures are compared in Fig. 2*b*. The comparison is made for a power supply of 155 A and 145 A in the top and bottom resistors, respectively. To have the cooling rate 10^{-2} K/s carefully controlled, a power down in the current intensity of $CI_{\mathrm{bottom}} = 7\times10^{-4}$ A/s for the bottom resistor and $CI_{\mathrm{top}} = 4.5\times10^{-4}$ A/s for the top resistor was applied. The difference in the rates of the electric current variaion was due to the difference in the design of the heating elements (i.e. resistors) in terms of the size and thickness. The temperature difference between the experimental and the simulated values at the thermocouples mentioned above is approx. 2.5 K during the solidification stage, whereas the temperature distribution is almost similar. With this acceptable difference between the experimental and simulated temperatures illustrated in Fig. 2*b*, the numerical model is considered to be a close representation of the experimental furnace. Similarly, for validation purposes, a full-scale Bitter coil (Fig. 3*a*) was manufactured to make an electromagnetic calculation using the Comsol MultiphysicsTM software. First, the radial component B_r of the simulated travelling magnetic field along the central axis ($R = 0$ mm) without the crucible and silicon charge was numerically calculated and compared with the experimental measurements, which were made for three different values of the same three-phase power supply 400, 600 and 800 A.

The comparison for the downward TMF presented in our previous study [7] clearly shows a good correspondence between the numerical results and those of the experimental measurements. Then the time-averaged $\langle F_{LTZ} \rangle$ was calculated by solving Maxwell's equations, and the extracted value was implemented into the CFD calculation. It was then weighted by the corresponding liquid phase volume fraction (f_{l}), and used as a source term in the momentum conservation equations. Fig. 4 presents the evolution of

(*a*) (*b*)

Fig. 3. (*a*) Image of the experimental setup of the Bitter coil used for the VB2 furnace; (*b*) its 3D reproductive geometry used in numerical simulation.

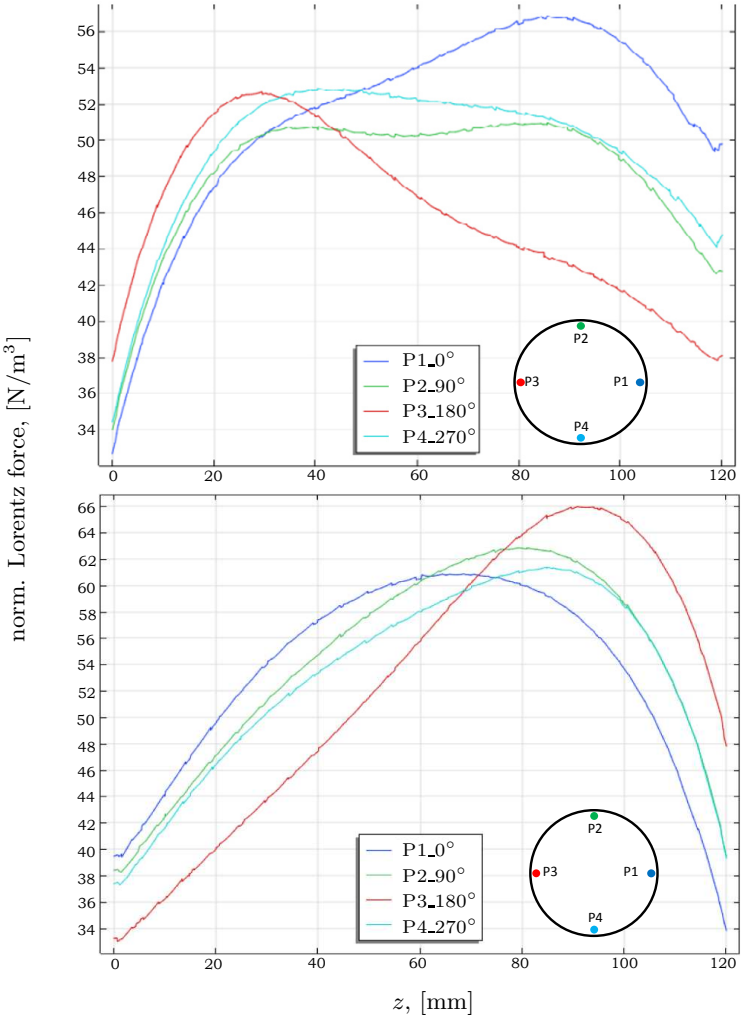

Fig. 4. Vertical evolution of the Lorentz force density averaged in time in the magnetic skin for the current $I_1 = I_2 = I_3 = 200$ A: (*a*) downward TMF, (*b*) upward TMF.

the Lorentz force magnitude averaged in time at different positions distributed in the azimuth plane at the level of the magnetic skin $\delta = 1$ mm. The numerical calculation of four positions in the azimuthal direction, namely, P1, P2, P3 and P4, is shown in Fig. 4. The results clearly illustrate that in both cases (downward and upward TMF), the vertical distribution of the Lorentz force is different from one position to another. However, there is some relative resemblance in the distribution of the Lorentz force between P2 and P4 for both cases. This behaviour may explain the presence of almost symmetry of the two loops in the YZ-plane and, hence, a concave or a convex solidification front, depending on the direction of rotation of the silicon melt related to the applied TMF direction. Moreover, the significant difference in the Lorentz force intensity distribution between P1 and P3 explains the appearance of only one dominant vortex in the XZ-plane and, therefore, the inclined curved shape of the solidification interface, which will be the subject of the next section.

4. Effect of TMF stirring on solidification.

To illustrate the TMF induced flow and its effect on the solidification front of silicon, the solidification sequence was analyzed for the 3D global geometry of the crucible and meridional vertical planes (XZ and YZ). Two cases of TMF stirring were examined: downward and upward. Schematic views of the liquid flow pattern and solidification process are shown for the case of downward stirring and similarly for the case of upward stirring in Fig. 5 one hour after the solidification began ($t = 3600\,\mathrm{s}$).

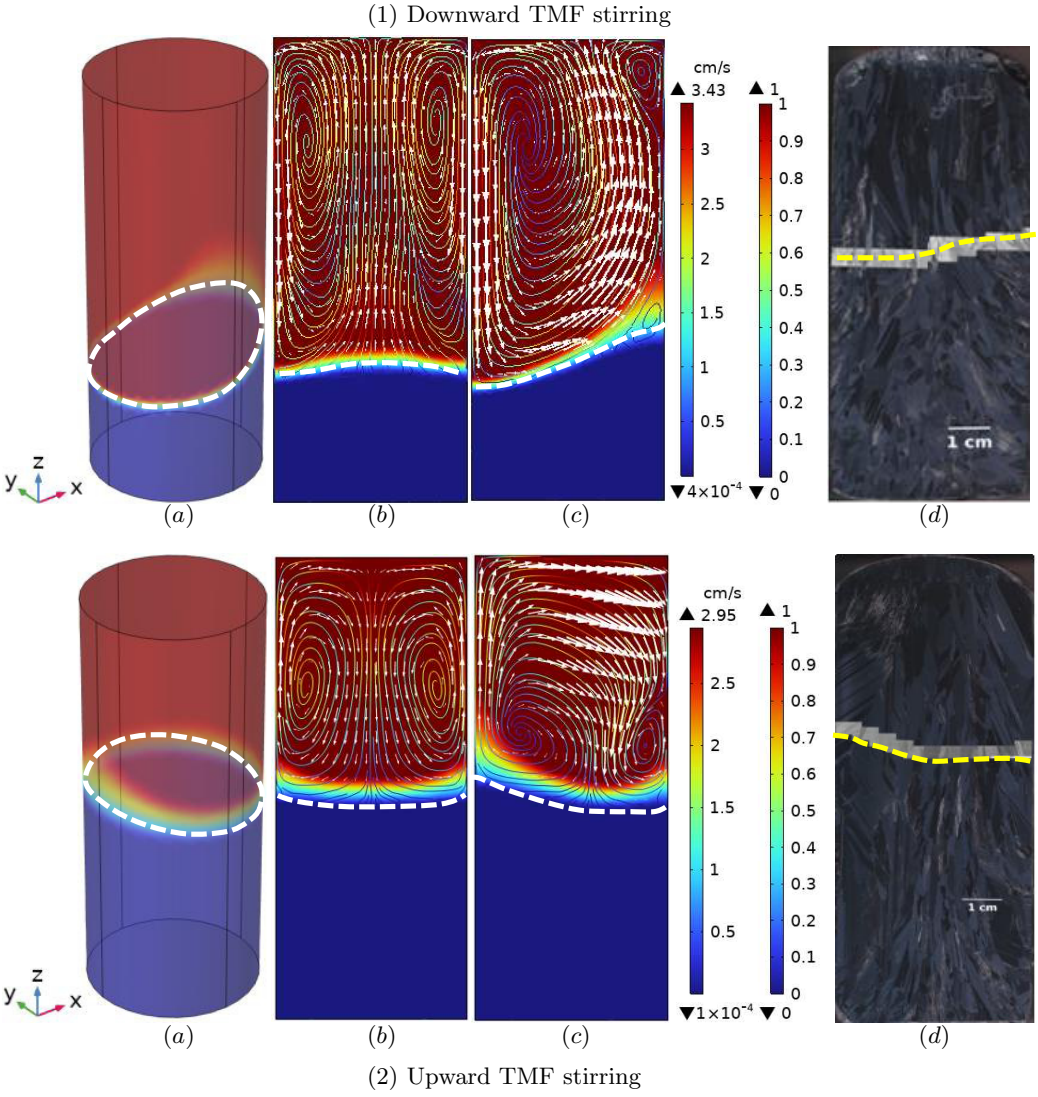

Fig. 5. Schematic views of the MHD liquid flow pattern at a chosen instant ($t = 1\,\mathrm{h}$). (1) TMF downward stirring; (2) TMF upward stirring. (*a*) 3D view; (*b*) YZ-plane; (*c*) XZ-plane, (*d*) solidification front of the corresponding experiment ingot slice in the XZ-plane under TMF stirring by Peltier electric technique [8]. Yellow dashed lines indicated the experimental interface, and dashed white lines indicated the numerical diffuse interface.

As expected, the Reynolds number $\mathrm{Rn} = \rho_l u_{max} L_c / \mu_l = 33423$, where $L_c = H^2/D$, H is the height and D is the diameter, estimated for maximum velocities equal to 3.4 cm/s for the downward and 2.9 cm/s for the upward flow clearly indicates that the flow is turbulent. As preliminary results show, the MHD flow generated by the Bitter coil significantly changes the usually expected axisymmetric torus-type MHD flow topology, which results in a distinct 3D flow configuration. Indeed, Fig. 5(1*b*) and Fig. 5(2*b*) show that in the YZ-plane the MHD flow configuration illustrates the possibility of almost symmetry of two loops with opposite rotation directions. However, in the XZ-plane Fig. 5(1*c*) and Fig. 5(2*c*)) both cases illustrate the appearance of one principal predominant vortex in the crucible a djacent to a secondary small one. For more details about the configuration of the resulting MHD flow the reader can refer to [7].

Fig. 5 shows also a comparison between the simulated solidification front and the corresponding experiments with the same configuration of TMF stirring. Satisfactory agreements between the measurements and the simulation results were obtained. The solidification front marked on the silicon ingot slices in Figs. 5(1*d*) and (2*d*) was revealed by the Peltier electric solid-liquid front detection technique [5]. It is clear that the flow pattern in the silicon melt significantly affects the shape of the solid-liquid interface and its evolution in space and time. Indeed, the solidification front after one hour of cooling demonstrates a remarkable progress for upward stirring compared to the downward case. Concave and convex shapes of the solid-liquid interface were obtained by the numerical simulation, as shown in Figs. 5(1*b*) and (2*b*) in the YZ-plane. However, the numerical results corresponding to the XZ-plane presented in Figs. 5(1*c*) and (2*c*) indicate that the solid-liquid interface corresponds to a shape of curvature leaning to one side according to the MHD flow configuration. This shape of curvature leaning to one side, characterizing the solidification interface in the XZ-plane, is in good agreement with the corresponding experimental silicon ingot slices displayed in Figs. 5(1*d*) and (2*d*) for both cases of TMF stirring (i.e. downward and upward TMF).

We can highlight some findings about the effect of the two different TMF stirring modes applied to the solidification process, particularly concerning the shape and the change of position in time and space of the solidification interface.

(1) The quasi concave or convex shape in the YZ-plane for the downward and upward modes of TMF stirring is the direct consequence of the direction of rotation of the convective loop created by electromagnetic stirring in the liquid phase.

(2) The relative dominance of the vortex located in the XZ-plane is responsible for the curvature leaning to one side of the solidification inreface.

(3) The relative delay in the solidification front progress for the downward TMF compared to the upward TMF can be attributed also to the electromagnetic stirring that exerts two main effects. First, the Lorentz force in the case of the downward TMF causes, therefore, a downward movement of the hot flows which will homogenize the pool and decrease the temperature gradients, thus creating unfavourable conditions for the solidification front progress. Second, the hot flow transported by convection impinging the solid-liquid interface under certain conditions can enhance the remelting of the latter, which in turn may cause the interface delayed progress.

5. Conclusions.

A full 3D numerical multidisciplinary model of the vertical Bridgman 2 inches (VB2) furnace was numerically investigated and experimentally validated. The used model has shown its effectiveness in predicting the behaviour of magnetohydrodynamic flow, thermal field configuration, phase change phenomenon and solid-liquid interface shape

and progression. Two configurations of the travelling magnetic field have been examined, i.e. downward and upward. Each TMF mode provides a specific configuration of electromagnetic forces leading to a particular hydrodynamic configuration in the silicon melt. The simulated 3D model illustrates clearly that MHD convection has a significant effect on the solid-liquid interface in terms of the shape and symmetry. It was found that the geometric shape of the solidification front does not exhibit a perfect concave or a convex shape. In the light of this preliminary numerical investigation, we can conclude that the irregular shape of the solidification interface, according to the azimuthal direction, is an indicative factor that could call into question the control of the solidification process. We believe that the designed Bitter coil and the current electromagnetic parameters used in the VB2 furnace can certainly initiate an adequate MHD flow in the melt, but remain ineffective to ensure carefully a controlled shape of the solid-liquid interface during the directional solidification process. For this purpose, the TMF apparatus obviously needs a set of adjustments in terms of the design and size. A particular electrical phase distribution and a different specific power supply for each phase which will be a motivation and an interesting subject of the future study.

References

[1] M. Cablea. *Numerical and experimental studies of magnetic field effects on solidification of metallurgical silicon for photovoltaic applications* (PhD Thesis, 2015, Grenoble University, France).

[2] T. Yoshikawa, K. Morita. Refining of silicon during its solidification from a Si-Al melt. *J. Crystal Growth*, vol. 311 (2009), pp. 776-779.

[3] N. Dropka, I. Buchovska, U. Degenhardt, Frank M. Kiessling. Influence of impurities from SiC and TiC crucible cover on directionally solidified silicon. *J. Crystal Growth*, vol. 542 (2020), 125692.

[4] K. Zaïdat, N. Mangelinck-Noël, R. Moreau. Control of melt convection by a travelling magnetic field during the directional solidification of Al-Ni alloys. *C. R. Mecanique*, vol. 335 (2007), no. 7-8, pp. 330335.

[5] M. Cablea, K. Zaidat, A. Gagnoud, Ab. Nouri and Y. Delannoy. Directional solidification of silicon under the influence of travelling magnetic field. *J. Crystal Growth*, vol. 401 (2014), p. 883.

[6] B. Hiba, Ab. Nouri, L. Hachani and K. Zaidat. 3D numerical simulation with experimental validation of a traveling magnetic field stirring generated by a Bitter coil for silicon directional solidification process. *IOP Conf. Ser.: Mater. Sci. Eng.*, (2022) 1223 012001.

[7] B. Hiba, Ab. Nouri, L. Hachani and K. Zaidat. Analysis of the symmetry of 3D silicon melts flow generated by a Bitter travelling magnetic field in a cylindrical crucible. *Magnetohydrodynamics*, vol. 58 (2022), no. 4, pp. 397-408.

[8] M. Cablea, K. Zaidat, A. Gagnoud *et al.* Multi-crystalline silicon solidification under controlled forced convection. *J. Crystal Growth*, vol. 417 (2015), p. 44.

[9] S. Molokov, R. Moreau, K. Moffat. *Magnetohydrodynamics* (Springer: Dordrecht, 2007, The Netherlands.)

[10] T. Wang, L. Hachani, Y. Fautrelle *et al.* Numerical modelling of a benchmark experiment on equiaxed solidification of a SnPb alloy with electromagnetic stirring and natural convection. *Int. J. Heat Mass Transf.*, vol. 151 (2020), p. 119414.

[11] F. Samara, D. Groulx and P.H. Biwole. Natural convection driven melting of phase change material: comparison of two methods. In: *Proc. the COMSOL Conference*, 2012.

[12] E.M. Robynne and D. Groulx. Modeling convection during melting of a phase change material. In: *Proc. the COMSOL Conference*, 2011.

[13] I. Sari, L. Hachani, A. Kharicha *et al.* 3D numerical simulation and experimental investigation of pure tin solidification under natural and forced convection. *Int. J. Thermal Sciences*, vol. 164 (2021), p. 106900.

Received 29.12.2023